INSTRUMENTATION

Digital Scintigraphy: Principles, Design, and Performance

Sebastian Genna, Sing-Chin Pang, and Andrew Smith

Boston Veterans Administration Medical Center, the Evans Memorial Department of Clinical Research, and University Hospital, Boston University Medical Center, Boston, Massachusetts

In a digital camera the position of a scintillation event is computed following analog-to-digital conversion of photomultiplier pulse charges. Digital position analysis is essentially a mathematical inversion procedure based upon calibrated responses of the photomultipliers to scintillations from a narrow-beamed source that maps a detector's field of view. Operationally, a camera's image characteristics are optimized by means of computer-generated inversion reference tables, individually tailored to the specific response characteristics of each detector. Design considerations indicate that cameras of varied configurations, e.g., linear, disc-shaped, rectangular, or cylindrical, can be analyzed by this method. Also, for any given electro-optical system, energy resolution, spatial characteristics, and event-rate performance can be made superior to analog systems. The measured performances of a one-dimensional test camera, although limited in its optical and electronic design, support this conclusion.

J Nucl Med 22: 365–371, 1981

Two decades ago Anger (*1*) taught us that the position of a scintillation event in a planar crystal could be determined by analysis of the quantitative partitioning of light among the elements in an array of photomultipliers. Conventionally, an event's position is computed by analog means from the analog responses of a camera's photomultipliers to a scintillation. In a new approach, scintillation position is computed digitally from digitally converted photomultiplier pulses (*2–7*).

In analog systems, the problems associated with nonisotropic, nonuniform, and nonlinear responses of photomultipliers to light scintillations are formidable. These problems generally manifest themselves as degraded position, resolution, and uniformity characteristics. Spatial tube response has generally been improved by adjusting the light-collection geometry—by techniques such as light-pipe shaping, surface reflection alterations, and optical maskings—and by providing nonlinear electronics such as threshold amplifiers (*8*) and delay-line (*9*) adjustments. It should be recognized that all of these procedures trade improved linearity and uniformity in tube response for diminished light collection, thereby limiting both spectral and spatial resolutions.

Digital position analysis is essentially an inversion procedure, based upon calibrated responses of a camera's photomultipliers to scintillation events as a function of their positions. Operationally, it consists of two parts: a *calibration part*, in which inversion reference tables are fabricated for each photomultiplier unit from its responses to calibration source events and *an analysis part*, in which these tables are referred to in order to determine the spatial origin of a scintillation event.

TEST CAMERA SYSTEM

Figure 1 illustrates schematically the detector elements of a digital test camera and a source-positioning apparatus used to calibrate it. The detecting crystal, which measures 33 cm long, 4 cm wide, and 1.25 cm thick, is coupled to a 1-cm-thick light pipe. Seven round

Received June 24, 1980; revision accepted Dec. 19, 1980.

For reprints contact: Sebastian Genna, PhD, Boston Veterans Administration Medical Ctr., 150 So. Huntington Ave., Boston, MA 02130.

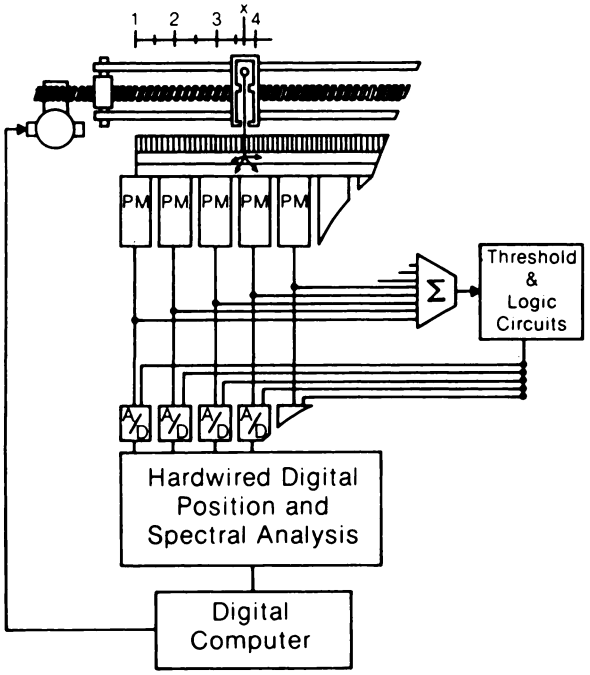

FIG. 1. Schematic of one-dimensional detector and source-positioning apparatus. Computer-controlled stepping motor positions gamma beam. Summed photomultiplier (PM) pulses are analyzed and selected by analog discrimination logics that trigger pulse integrations and digital conversions (A/D). Calibration is by means of a digital computer while event analysis uses a hardwired digital system.

photomultipliers, diameter 2 in., are mounted on 5.3-cm centers in a linear array on the collecting surface of the NaI(Tl) crystal/light-pipe assembly. By this means six surface segments (one between each pair of adjacent photomultipliers), comprising ~25% of the area of the mounting plane of the light pipe, remain uncoupled to photocathode light collectors. These regions and all other external optical surfaces are made highly reflective by standard means. No light masking or other reflection-altering procedures for adjusting light-collection characteristics are used. Reflecting surfaces between photomultipliers and the detector edges are known to degrade their spatial responses, ultimately resulting in degraded spatial resolution and uniformity. Consequently, this test geometry presents unusual optical problems.

System electronics consist of: (a) analog NIM* discriminators and logic circuits, which are used for fast (6-nsec) threshold discriminations of summed dc-coupled photomultiplier signals in order to provide pulse-pileup rejections and to gate the integration intervals of selected pulses; (b) seven pulse-integrating sample-and-hold circuits (one for each photomultiplier), each of which is coupled to a 10-bit, 1-μsec analog-to-digital converter; (c) digital electronics, designed and built for energy and position analyses with through-put capabilities in excess of 160 kilo-events per second; and (d) a digital computer for calibration and process control.

During the separate integration of the photomultiplier pulses, quantitative pulse-charge errors are produced when substantial parts of two or more pulses occur within the pulse-integration time of the sample-and-hold circuitry. These pulse-pileup errors, which occur at high count rates, distort spectral and spatial analyses. The test camera system uses conventional delay-line clipping (*10*) to achieve faster baseline recovery and fast discriminator logic circuitry to reject pileup before digital analysis. The analog analysis ultimately accepts pulses of interest that lie within preselected analog upper- and lower-level discriminators and are not rejected by pulse-pileup criteria. Thereafter, each photomultiplier pulse is subject to pulse integration, over a 400-nsec interval, and digital conversion. Integration and digital conversion take approximately 1.7 μsec. The analog system is dead during this interval and the pulse is allowed to decay before another pulse is accepted. A subsequent position-dependent digital single-channel analysis of the pulse charge is effected by the digital electronic circuitry. This provides a more restrictive and accurate photopeak window and additional rejection of events, to which secondary pulses contribute, that are not otherwise rejected by analog discrimination means. This window is more accurate because: (a) it accounts for spatial variation of the energy pulse signal, and (b) pulse analysis is more reliable statistically after pulse integration.

As a first step, before any calibration or analysis procedure, the seven photomultiplier gains are adjusted automatically through the use of computer control of the position of a calibrating source and of the high voltage of each photomultiplier. These controls are performed with the aid of a modular "Computed Automated Measurement and Control" (CAMAC) system. For these adjustments, a narrow beam (1 mm diam.) from a Tc-99m ray source is projected sequentially to positions normal to the crystal detector on tube centers. With the source at each of the seven tube centerline positions, the digitally converted signals are summed for each of a statistically significant number of scintillation events to obtain a spectral distribution of the summation of pulse charges. A computer routine then finds the centers of the photopeaks of these spectra and, for each excursion across the set of seven photomultipliers, adjusts the high voltages of the seven tubes, interdependently, seeking convergence of the peak centers. The process is repeated until convergence is achieved to within ±1% (usually two to three excursions). This procedure establishes, with little time or effort, retrievable standard conditions for calibration or analysis.

CALIBRATION AND POSITION ANALYSIS

Calibration is also performed through the use of the digital computer. The function of this procedure is to examine the response characteristics of each photo-

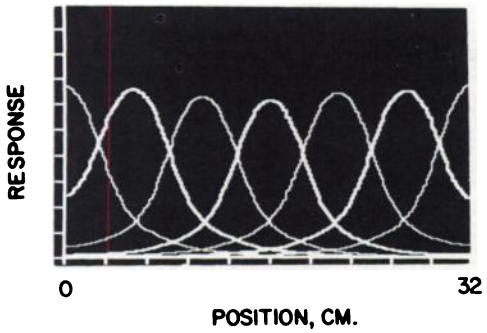

FIG. 2. Normalized photomultiplier response characteristics. Ordinate is average normalized response (fractional pulse charge averaged over 400 events per location) from each of seven photomultipliers as a function of position, x, of calibrating source.

multiplier to source events at prescribed positions and thereby to fabricate reference tables through which position data may be supplied as a function of tube responses. Position analysis is performed by the hardwired digital circuitry, the function of which is to compute position and construct an image, at a rapid rate, through table look-up procedures.

In order to calibrate the camera, the source is positioned along the x axis (Fig. 1) in 1.25-mm intervals. At each position, pulse responses from each photomultiplier to scintillations from the gamma beam are then sampled, integrated, and digitally converted. Each signal is then normalized by dividing it by the sum of all digital signals deriving from the same event. These normalized responses, denoted by z_i, where the subscript refers to the photomultiplier, are the raw data for point-by-point calibration of the linear camera.

Figure 2 illustrates the normalized response characteristics of the seven photomultipliers. Each point on a curve is the average normalized response, $\bar{z}_i$, of a statistically adequate number of events produced at the specified calibration positions. Each tube's response function is a bell-shaped curve having a half-width ~25% larger than the tube-separation distance. Within the limitations of the statistical uncertainties in tube responses and the spatial double-valuedness of the responses of tubes removed from the detector edges, each tube can provide a separate determination (though interdependently connected by the normalization constraint $\sum_i z_i$ = constant) of a probable position of a scintillation event, $x_i(z_i)$, from its evoked response, z_i. The double-valuedness may be removed partially by a computational routine that identifies the tube with the highest response to an event and then compares the relative responses of its two neighbors to determine whether the event occurred to the left or right of the highest responding tube.

The uncertainties in the tube-response functions may be appreciated better by reference to Fig. 3, which schematically shows an expanded re-illustration of the responses in the vicinity of the second tube, along with

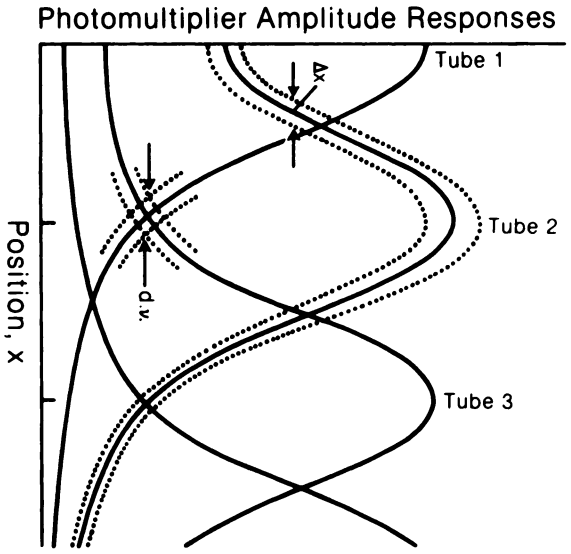

FIG. 3. Schematic illustration of normalized photomultiplier responses in vicinity of second tube, along with their uncertainty envelopes. At some distance from tube center, position uncertainty may be set inversely proportional to error envelope's width, Δx. Near a tube center, however, residual double valuedness (d.v.) must also be accounted for.

the uncertainty envelopes. At some distance from a photomultiplier center, the reliability of an $x_i(z_i)$ determination evoked by a z_i signal may be set equal to the reciprocal of the uncertainty at that point $w_i(z_i) = 1/\Delta x_i(z_i)$. However, if the source is near the center of a tube, a residual double-valuedness uncertainty also exists thereabouts even after the removal routine outlined above. The magnitude of this uncertainty is indicated by the intersections of the error envelopes of the adjacent two tubes. This residual error adds to statistical uncertainties near tube centers in a complex manner.

From the set of z_i tube responses evoked by a scintillation event, the probable position $\langle x \rangle$ of the event can be equated to a linearly weighted average of the separately determined $x_i(z_i)$, where the weighting functions are proportional to the reliability $w_i(z_i)$ of the $x_i(z_i)$ determination, i.e.,

$$\langle x \rangle = \frac{\sum_i w_i(z_i) x_i(z_i)}{\sum_i w_i(z_i)} \qquad (1)$$

One method of obtaining reliability factors, w_i, which takes the effect of residual double-valuedness uncertainty into account, is as follows.

1. From the spatial response curve of each tube, a spatial look-up table is constructed, whereby x_i is extracted for each z_i referenced. (Small modifications are made to these tables to account for z_i values not otherwise performed: modifications that place z_i responses greater than the peak value of a curve at the center of the curve, and the same for lower values at the edges.)

2. The source is then scanned incrementally across the detector field.

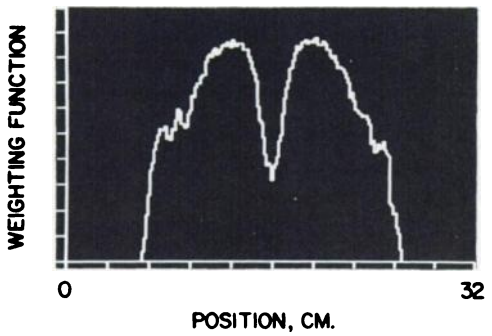

FIG. 4. Reliability weighting function from central photomultiplier, shown as function of calibrating source's position, x. Near center of tube, reliability is low, reflecting residual double-valuedness (primarily) and poor statistics.

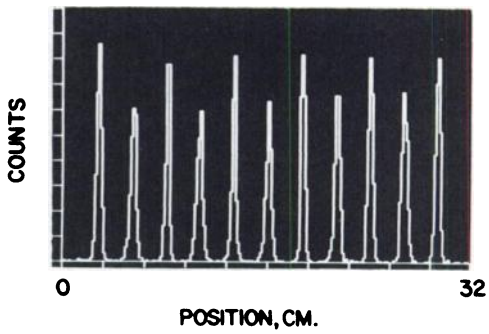

FIG. 5. Spread images of narrow-beamed source, 1 mm diam., positioned at tube centers and mid-way between them. The point spread functions derived therefrom varied from a low value of 3.5 mm FWHM to a high value of 5.0 mm FWHM.

3. At each incremental position, x, the double-valuedness routine makes a determination as to whether a scintillation event is to the left or right of the tube center involved.

4. Based upon this determination, $x_i(x)$ is extracted for each z_i from a scintillation event.

5. From a large number of these $x_i(x)$ determinations, one of two alternative procedures for calculating $w_i(x)$ is chosen: (a) if the distribution of $x_i(x)$ is continuous (no residual double-valuedness), $w_i(x)$ is set equal to the fractional number of $x_i(x)$ that fall within a spatial window, Δx, centered about the position of the source, x; or (b) if the distribution is double-valued, $w_i(x)$ is assigned an empirically adjustable low value.

Figure 4 shows an experimental result of such a determination for one photomultiplier. Functions such as this are the weighting functions used in Eq. 1 for position analyses. Finally, from the response function (Fig. 2) and weighting function (Fig. 4), the inverse functions $x_i(z_i)$ and $w_i(z_i)$ are obtained for each photomultiplier. The digitized $w_i(z_i)$ and a weighted spatial function defined by $S_i(z_i)=w_i(z_i)x_i(z_i)$ are calculated and stored in reference tables as functions of z_i. The product $S_i(z_i)$, rather than $x_i(z_i)$, is tabulated to conserve subsequent computation time. Except for the two bounding tubes, double-valuedness is accounted for by constructing, for each tube, two tables that may be referenced selectively by z_i signals identified to occur to the left or right of a tube center.

Digital position analysis is performed in accordance with Eq. 1. Digitally converted pulse integrations are stored in seven buffer memories (one for each photomultiplier) that derandomize accepted events. Subsequent hard-wired analysis routines (a) sum the integrations and normalize each signal to obtain z_i responses; (b) remove spatial double-valuedness, as discussed; (c) refer to appropriate z_i tables and extract $S_i(z_i)$ and $w_i(z_i)$ for all values of i; (d) sum these extracted function values and compute the probable position, $\langle x \rangle$, of the event from Eq. 1; (e) perform position-dependent sliding-window single-channel discrimination of the summation signal; and (f) deposit $\langle x \rangle$ in an image matrix if digital pulse discrimination did not reject the signal. More than one image matrix may, in principle, be provided by sorting events in accordance with the passings of two or more digital single-channel analyzers. The digital computer is used for subsequent processing and display of the recorded image.

RESULTS

Figure 5 illustrates spread functions obtained with the narrow-beamed source, 1 mm in diameter, which was positioned sequentially at the centers of tubes and mid-way between them. Inherent spatial resolution distances varied from a low value of 3.5 mm FWHM, between tubes, to a high of 5.0 mm FWHM at their axes. This oscillatory behavior, which is predictable from the tube characteristics, averaged less than 4.2 mm FWHM over all. Linearity was evaluated by comparing the average of the measured values, $\langle \bar{x} \rangle$, for 400 events, with the actual source positions, x, for all points (in 1.25-mm increments) within 90% of the camera's field of view, i.e., 90% of the distance between the centers of the end tubes. Figure 6 shows the results of these measurements.

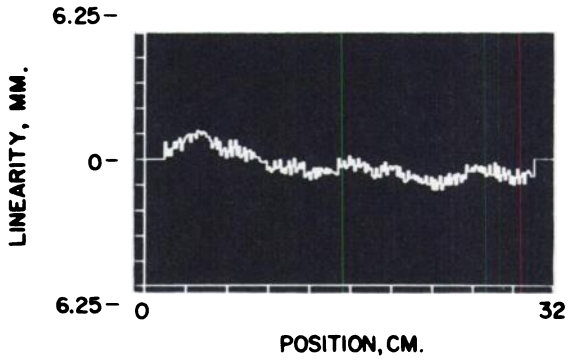

FIG. 6. Linearity of analyzed position $\langle x \rangle$ as a function of actual source position, x. Ordinate equals the difference, $x-\langle \bar{x} \rangle$, where each $\langle \bar{x} \rangle$ is average of large number of determinations with source at x.

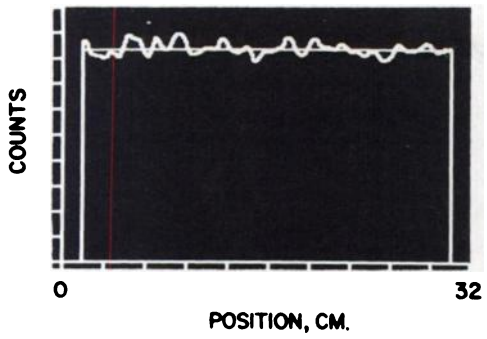

FIG. 7. Pixel-by-pixel camera uniformity after convolution with a weighted smoothing function having half-width of 5.0 mm. Uniformity is specified over 90% of camera's field of view in 1.25-mm pixel widths.

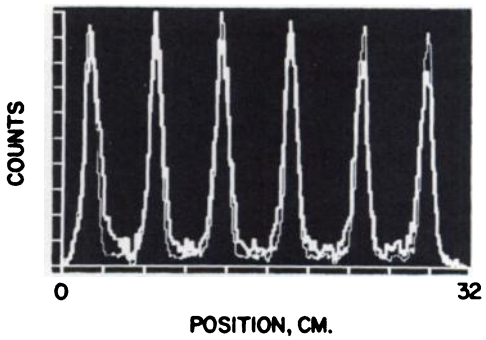

FIG. 9. Two superimposed images of set of six Tc-99m sources as in Fig. 8. The valley-to-peak ratios at the high event rate (110 kcps, light lines) were about 3% higher than those at a low event rate (2.0 kcps, heavy lines) because of residual pulse pileup.

Maximum deviations of this comparison were ~1.2 mm, and the average deviation was 0.5 mm. Uniformity characteristics were obtained by scanning the gamma source over the camera field. Figure 7 shows results after convolution with a linear smoothing function having a half-width of ~5 mm. The average and maximum deviations from constancy are ±2.1% and ±6.3%, respectively.

Event-rate characteristics were interpreted with the use of a discrete-source configuration phantom. This phantom has the same scatter geometry as the phantom reported by Adams, Hine, and Zimmerman (*11*), which was designed to simulate in vivo cardiac scatter characteristics. The phantom consisted of a set of six Tc-99m sources (each contained in a plastic test tube 1 cm in diameter) positioned in a water phantom at separations of 5 cm along a line parallel to the detector's plane. Five centimeters of water were in front of the source centers and 10 cm behind. Figure 8 illustrates the event-rate characteristics of the digital camera, using the phantom in conjunction with a 30% window centered about the photopeak. Figure 9 shows two images; one at the maximum event rate (110,000 cps) and one at a low rate (2,000 cps). These show negligible differences in the widths of the images of the 10-mm sources (about 12.5 mm FWHM). However, the valley-to-peak ratios differ by a few percent of the peak height. Similar measurements with a 20% window yield a maximum event rate of about 84,000 cps.

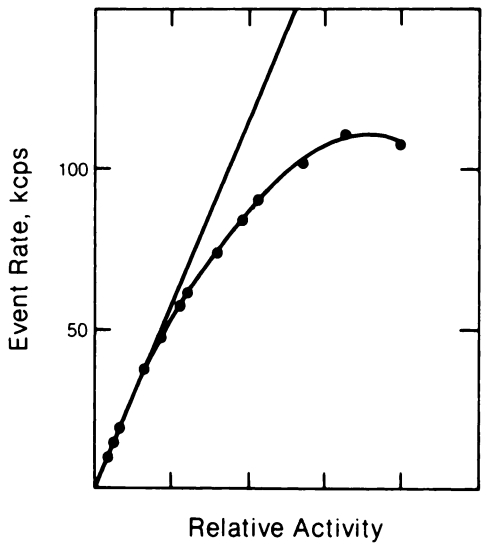

FIG. 8. Event-rate characteristics of digital camera using water phantom containing a set of six Tc-99m sources and a 30% digital photopeak window. Sources are contained in six 1.0-cm plastic test tubes positioned in water at 5.0 cm separations along a line parallel to NaI(Tl) crystal. Five centimeters of water were in front of source centers and 10 cm were behind.

DISCUSSION

A basic justification for digital position analysis would be the claim that *for a given camera configuration* spatial and temporal characteristics can be made superior. Conceptually, it should be evident that, given a set of photomultiplier responses that may have some nonlinear or nonhomogeneous components, a system may be "tuned" to perform better by tailoring digital inversion tables to fit individual tube characteristics than by less flexible analog means. Also, it appears possible that light-attenuating procedures (masks, etc.) may be completely avoided, resulting in higher spectral and, possibly, spatial resolution.

The performance characteristics reported herein are not the optimum obtainable by digital position analysis. Indeed, with the present test system, configurational changes would significantly benefit performance—changes such as the use of square photomultipliers to reduce the areas of inter-tube reflection surfaces or the use of a thinner crystal. There is also evidence that event-rate characteristics may be improved by modification of the pulse-pileup rejection logic. Also, the 1.7-μsec interval currently required for pulse integration and digital conversion is unnecessarily long and limits the rate of events that can pass through the analog pulse-height window and enter the digital hardware. Pulse integration sample-and-hold times and digital

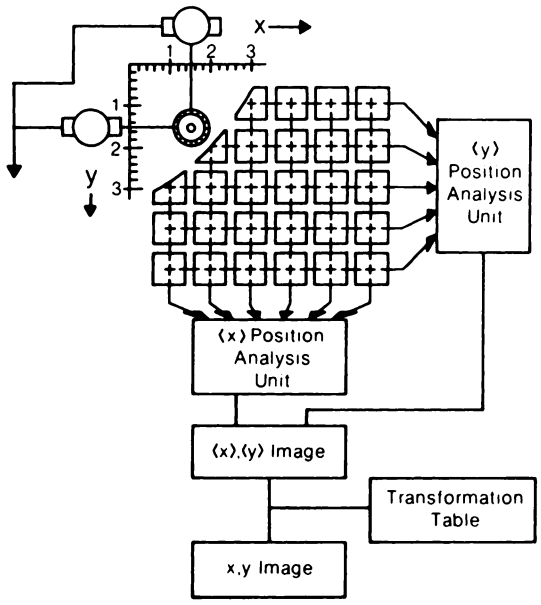

FIG. 10. Schematic diagram of square digital scintillation camera. Computer-controlled stepping motors position narrow-beamed radiation source to map camera's Cartesian field of view. Calibration is by means of a digital computer. Analog discrimination and logic unit (not shown) gates the row-and-column sets of photomultipliers for parallel pulse integration and conversion. Separate x and y hardwired position units provide coordinate-independent image ⟨x⟩, ⟨y⟩. Subsequent transformation by digital computer provides a coordinate-interdependent image, x, y.

conversion times may be reduced to about 1.0 μsec by providing each photomultiplier with dual dedicated integration-conversion circuits that are alternately addressed. The higher event rates made possible by this signal-sharing modification will also require faster digital position- and spectral-analysis circuitry. A throughput rate in excess of 500 kcps is readily achievable with minor design and component modifications. An analysis of such a system and preliminary mock-up experiments lead us to expect that under typical cardiac scattering conditions, such as were simulated with our test phantom, an event rate of about 200 kcps will be achievable with a 30% window.

It is also germane to outline approaches to two-dimensional scintigraphy in order to relate the design and performance characteristics of the test camera to two-dimensional cameras, one of which is in a preliminary state of development. The methods of calibration and position analysis for two dimensions are, for the most part, similar to the one-dimensional methods. These may be explained by referring to the schematic drawing of a square scintillation detector and a two-dimensional Cartesian source-positioning apparatus as illustrated in Fig. 10. The photomultipliers are arranged in a row-and-column array, with the output signals of each row and column summed separately. These provide x and y positioning signals. The position responses in the x direction (keeping y constant) and in the y direction (keeping x constant) characteristically should be the same as those deriving from the one-dimensional system of Fig. 2. The responses are complicated, however, by the spacing between photomultiplier photocathodes and nonuniformities in photomultiplier or optical characteristics in each row or column. Thus, the x response curves and the y response curves may exhibit interdependence on their orthogonal coordinates.

To account for x and y interdependence, system calibration and subsequent position analysis each consist of two parts. In the first part, calibration and analysis proceed as though the 2-D system consists of two independent 1-D systems. Thus, for example, the columnar signals are used to construct x position with one minor modification. Since the x response is not truly independent of y, the tables derive from the average response (over all y) of each columnar set of photomultipliers, and vice versa for the row sets. Functional interdependence of the x and y coordinate responses may be accounted for through the use of a 2-D transformation table constructed by a second calibration procedure in which the narrow-beam source, illustrated in Fig. 10, is caused to map the square detector field in prescribed cartesian increments. At each point, a statistically adequate number of signals from events at each position are analyzed to obtain an average position $\langle\bar{x}\rangle$, $\langle\bar{y}\rangle$, at each of the x, y positions at which the source is located. From these data, a matrix conversion table is constructed,

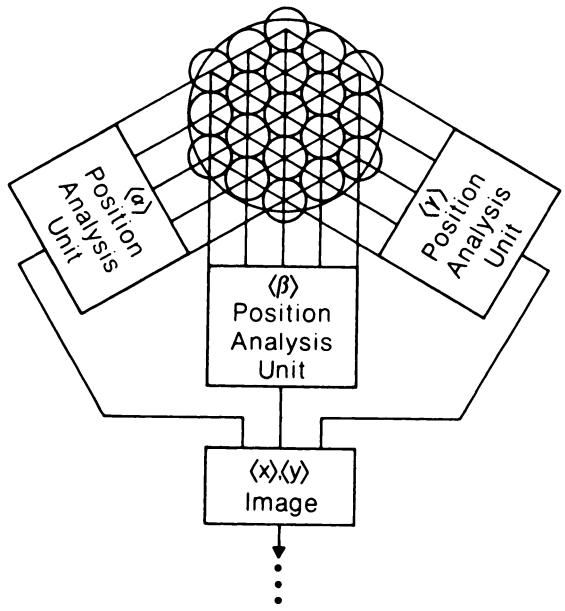

FIG. 11. Schematic of digital scintillation camera having circular disc detector and hexagonal array of photomultipliers. Because of symmetry, more information is gleaned by forming an image from triaxial redundant coordinates, ⟨α⟩, ⟨β⟩, and ⟨γ⟩. Cartesian coordinates, ⟨x⟩, ⟨y⟩, are obtained by trigonometric transformation. Thereafter, a coordinate-interdependent image is obtained by tabular transformation (not shown) based on two-dimensional calibrations.

giving values of the actual source position, x, y, for each evoked ⟨x⟩, ⟨y⟩ address referenced.

Methods for detectors having other configurations proceed similarly. In a cylindrically shaped detector, in which the photomultipliers are positioned along columns and rings (*2*), the procedure would be identical except that cylindrical coordinates describe the motions of the calibration source and the subsequent event positions and reference tables. For the conventional circular-disc planar detector, it is advantageous to adopt a triangular nonorthogonal redundant coordinate system (not completely redundant information) having axes along the three sets of rows in the hexagonal array of photomultipliers. Figure 11 illustrates this case. Three one-dimensional linear analyses from α, β, and γ look-up tables give the coordinates ⟨α⟩, ⟨β⟩, and ⟨γ⟩, respectively, that transform geometrically to ⟨x⟩, ⟨y⟩. Subsequent 2-D image transformations to remove one-dimensional interdependence are the same as for the square camera.

CONCLUSION

It is evident that digital scintillation cameras have performance potentials in excess of conventional analog systems. A one-dimensional camera, which was by no means designed for optimum optical performance, demonstrates spatial characteristics at least comparable to those of state-of-the-art of conventional systems. In two-dimensional digital cameras, spatial nonuniformities and nonlinearities should reduce to even much smaller levels, because of the imposition of a calibrated two-dimensional transformation table in addition to the independent one-dimensional procedures. Also significant are the potentials of single-crystal digital scintillation cameras to achieve event-rates comparable to those of multicrystal cameras.

FOOTNOTE

* NIM (Nuclear Instrument Modules) in an international analog nuclear-instrument standard.

ACKNOWLEDGMENT

This work was supported by the Veterans Administration Medical Research Services.

REFERENCES

1. ANGER HO: Scintillation camera. *Rev Sci Instr* 29:27-33, 1958
2. GENNA S, PANG SC: Application of fan reconstruction geometries to transmission and emission systems. In *Reconstruction Tomography in Diagnostic Radiology and Nuclear Medicine*, Ter-Pogossian MM, Phelps ME, Brownell GL, et al., Eds. 1977, pp 139-154
3. GENNA S, PANG SC: Analysis of an arcuate gamma camera design for transaxial reconstruction. In *Medical Radionuclide Imaging*. Vienna, IAEA, 1977, pp 323-334
4. GENNA S, PANG SC: Analysis of resolution and uniformity characteristics of a digital camera. Program, RSNA Annual Meeting, 215, 1978 (abst)
5. GENNA S, PANG SC: Design and performance of a digital camera. *J Nucl Med* 20:628-629, 1979 (abst)
6. GENNA S, PANG SC: U.S. Patent 4,095,107
7. GENNA S, PANG SC: U.S. Patent 4,228,515
8. KULBERG GH, VAN DIJK N: Improved resolution of the Anger scintillation camera through the use of threshold preamplifiers. *J Nucl Med* 13:169-171, 1972
9. HIRAMOTO T, TANAKA E, NOHARA N: A scintillation camera based on delay-time conversion. *J Nucl Med* 12: 160-165, 1971
10. BLATT SL, MAHIEUX J, KOHLER D: Elimination of pulse pileup distortion in nuclear radiation spectra. *Nucl Instr Meth* 60:221-230, 1968
11. ADAMS R, HINE GJ, ZIMMERMAN CD: Deadtime measurements in scintillation cameras under scatter conditions simulating quantitative nuclear cardiography. *J Nucl Med* 19:538-544, 1978